Post-depositional REE mobility in a Paleoarchean banded iron formation revealed by La-Ce geochronology: A cautionary tale for signals of ancient oxygenation

P. Bonnand, S.V. Lalonde, M. Boyet, C. Heubeck, Martin Homann, P. Nonnotte, Ian Foster, K.O. Konhauser, I. Köhler

Post-depositional REE mobility in a Paleoarchean banded iron formation revealed by La-Ce geochronology: A cautionary tale for signals of ancient oxygenation

P. Bonnand[1], S.V. Lalonde[2], M. Boyet[1], C. Heubeck[3], M. Homann[2,4], P. Nonnotte[2], I. Foster[2], K.O. Konhauser[5], I. Köhler[3,6]

[1] Laboratoire Magmas et Volcans, Université Clermont Auvergne, CNRS, IRD, OPGC, F-63000 Clermont-Ferrand, France

[2] CNRS-UMR 6538 Laboratoire Géosciences Océan, European Institute for Marine Studies, Technopôle Brest-Iroise, 29280 Plouzané, France

[3] Department of Geosciences, Friedrich-Schiller-University Jena, Jena 07749, Germany

[4] Department of Earth Sciences, University College London, 5 Gower Place, WC1E 6BS London, UK

[5] Department of Earth and Atmospheric Sciences, University of Alberta, Edmonton, Alberta T6G 2E3, Canada

[6] Geozentrum Nordbayern, Friedrich-Alexander University Erlangen-Nürnberg, 91054 Erlangen, Germany

*Corresponding Author: *pierre.bonnand@uca.fr*

Abstract

Precambrian banded iron formations (BIF) are chemical sedimentary deposits whose trace element signatures have been widely used to interrogate the chemical composition and redox state of ancient seawater. Here we investigated trace element signatures in BIF of the 3.22 Ga Moodies Group, Barberton Greenstone Belt (South Africa), which are interbedded with near-shore siliciclastic sedimentary rocks and represent one of the oldest known shallow-water occurrences of BIF. Unusual rare earth element signatures, notably with pronounced negative Ce anomalies in shale-normalized spectra, have been previously reported for chemical sediments of the Moodies Group, which we confirm here through an expanded dataset for Moodies BIF spanning three different localities. We find negative Ce anomalies as low as 0.2 Ce/Ce* that are associated with unusual enrichment of LREE relative to HREE in the sample set. While total REE abundances and certain REE features appear strongly related to the concentration of detrital indicators (e.g., Zr), and are likely primary, other features, notably LREE enrichment, cannot be explained as a primary feature of the sediment. This is better explained by later addition of REE from a LREE-enriched but Ce-depleted fluid that generated the significant negative Ce anomalies observed in surface samples of Moodies Group BIF. This REE addition event influenced both Sm-Nd and La-Ce isotope systematics, the latter yielding an isochron of 60 ± 32 Ma, thus constraining the timing of emplacement of the negative Ce anomalies to the past 100 Ma, possibly upon surface exposure of the Barberton Greenstone Belt to wetter conditions during the Cenozoic. Our findings constitute a cautionary tale in that even the most immobile elemental redox proxies may be more sensitive to post-depositional modification than previously thought, and demonstrate the clear advantage offered by paleoredox proxies coupled to radiometric geochronometers to enable the direct dating of ancient signals of Earth surface oxygenation.

Keywords: Trace element signatures, Ce anomalies, La-Ce geochronology, rare earth element mobility.

1. Introduction

Banded iron formations (BIF) are chemical sediments deposited throughout much of the Precambrian. They consist primarily of iron oxide minerals (hematite, magnetite) and cryptocrystalline quartz (chert), along with lesser amounts of carbonates, iron-rich clays, and other secondary alteration minerals, depending on the metamorphic grade (Bekker et al., 2010; Konhauser et al., 2017). The precursor chemical minerals thought to have initially formed BIF (amorphous Fe(II)- and Fe(III)-hydroxides, carbonates, and silicates) are unstable, and have universally recrystallized to a more stable metamorphic assemblage of dehydrated minerals. Nonetheless, BIF have been widely considered a useful proxy for the chemical composition of ancient seawater and porewaters in which they formed (see Konhauser et al., 2017, for review). Being highly non-porous and impermeable, BIF are conventionally thought to be relatively robust against significant disturbance during metamorphism or metasomatism (e.g., Robbins et al., 2019a. Indeed, millimeter scale variations in trace elements (e.g., Bau, 1993; Bau and Dulski, 1996) and in iron isotope compositions in BIF (e.g. Frost et al., 2007), along with experiments simulating BIF diagenesis (e.g. Posth et al., 2013), have been used to argue for general elemental immobility, even for samples that have experienced complete recrystallization during amphibolite-facies metamorphism.

Rare earth element (REE) patterns, and in particular anomalies in the abundance of cerium (Ce) relative to its neighbors, are commonly used to interrogate redox conditions of ancient seawater. Cerium is particularly prone to fractionation from other REE because oxidation of Ce(III) to Ce(IV) under mildly oxidizing conditions greatly reduces Ce solubility, resulting in its preferential removal from solution onto Mn(IV)-Fe(III)-oxyhydroxides, organic matter, and clay particles (Byrne and Sholkovitz, 1996). Under oxidizing conditions, seawater is thus

characterized by a strong negative Ce anomaly. Accordingly, the presence of negative cerium anomalies in chemical sediments has often been used to infer oxidative conditions during deposition. Despite the potential for significant insight into the primary REE chemistry of ancient seawater, the interpretation of cerium anomalies in ancient sedimentary rocks requires caution. Post-depositional REE modifications have been described in several studies, showing that cerium may behave differently from other REE (Mongelli et al., 1993; Cotton et al., 1995). Hayashi et al. (2004) were the first to use La-Ce isotope systematics in an attempt to constrain the timing of emplacement of a cerium anomaly in ancient sedimentary rocks. Ce-138 is produced by the decay of ^{138}La ($T_{1/2}$=292.5 Ga). The use of ^{138}La–^{138}Ce systematics is challenging because of the long half-life of ^{138}La but is extremely powerful for dating La/Ce fractionation. The first La-Ce isotope measurements obtained by Hayashi et al. (2004) on samples from the Barberton Greenstone Belt (BGB) show that the presence of cerium anomalies must be interpreted with caution. They attributed Ce anomalies in the BGB, including a single BIF sample from the Moodies Group with Ce/Ce* = 0.93 (calculated by Hayashi et al. in the absence of Pr data as the chondrite-normalized projection between La and Nd) to post-depositional remobilization of REE prior to ca. 1.1 Ga (Hayashi et al., 2004).

In this paper we present major and trace element measurements in 48 BIF outcrop samples collected at three localities in the Moodies Group, dated at 3.22 Ga (Heubeck et al., 2013). Measurements of the La-Ce and Sm-Nd isotope systematics are presented in samples characterized by a large range of cerium anomalies. This dataset permits (1) direct dating of the formation of the cerium anomaly, and (2) to resolve whether REE spectra represent primary features or were later modified during secondary events, such as surficial weathering of exposed outcrop. Here we demonstrate that the negative cerium anomalies in Moodies BIF were produced

by relatively recent fluid addition and that this signature cannot be used to discuss redox conditions during their deposition.

2. Geology of Moodies Group BIF

The Moodies Group of the BGB is comprised of approximately 3.5 km of sand- and siltstone, subordinate conglomerate and volcanics, and minor ferruginous sediment that were mostly deposited in shallow-water and terrestrial settings (Heubeck, 2019). Dacitic volcanics conformably underlying basal Moodies strata are 3225±3 Ma old (Kröner et al., 1991). The onset of Moodies sedimentation is further constrained by a 3223±1 Ma age for a dacitic tuff in the uppermost Schoongezicht Formation of the underlying Fig Tree Group (Heubeck et al., 2013). Dacitic ash-fall tuffs in the central BGB, approximately mid-section in the stratigraphic column (near the BIF unit MdI2, Figure 1), yield an age as low as 3219±3 Ma (Heubeck et al., 2013), similar to a porphyritic dike crosscutting the topmost Moodies units dated at 3219±9 Ma (Heubeck et al., 2013). Thus, Moodies deposition occurred between 3223 and 3219 Ma, and likely within a few Ma of 3222 Ma ago (Heubeck et al., 2013). Regional metamorphic grade is lower greenschist facies (Tice et al., 2004), with evidence for metamorphic overprint during emplacement of the Kaap Valley Pluton at 3214 ± 4 Ma, during late granite plutonism at ca. 3100 Ma (Toulkeridis et al., 1994), and related to fluid circulation associated with Ventersdorp Supergroup volcanism or the Limpopo orogeny at ca. 2650-2700 Ma ago (Toulkeridis et al., 1998).

In the north-central part of BGB, up to four regionally mappable ferruginous units, 2 to 6 m thick and comprised of jaspillite and BIF, are interbedded with fine-grained sand- and

siltstones (Heubeck and Lowe, 1994). Geological mapping and interpretation of sedimentary structures suggest that deposition of ferruginous units occurred largely in prodelta- and protected bay / lagoonal settings. The BIF samples examined in this study were collected from surface outcrops at three localities in the Moodies Group (Figure 1); (1) unit MdI2 in the Clutha Creek section of the Eureka Syncline (CC; 25°41'52.81"S, 31°5'10.89"E), (2) unit MdI2 from the Devil's Staircase Road section of the Moodies Hills Block (DSR; 25°49'55.82"S, 31°0'50.49"E), and (3) unit MdI1 from the Stolzburg Syncline (SB; 25°54'8.04"S, 30°50'44.90"E). Samples were collected using hammers, chisels, and a sledge, avoiding clear signs of alteration, trimmed for fresh surfaces, and fractured pieces were discarded. All are distal from hydrothermally overprinted brittle-ductile shear zones that are common in the northern BGB. In all three sections, BIF occur in thick, conformable sections of thinly bedded, small-scale-slumped siltstones and very-fine-grained sandstone interbedded with rare laminated shale. See supplemental materials for a more detailed description of each sample site, including photos of the localities and of selected hand samples, as well as a lithological column for the DSR site situating the samples in stratigraphic context.

3. Methods

All samples were prepared using trace-element clean methods (crushing and powdering in pure tungsten carbide and agate, respectively) and all digestions and column separations were performed in clean laboratories at the European Institute for Marine Studies in Brest and at the Laboratoire Magmas et Volcans located at the Université Clermont Auvergne, France. For analysis of major elements, samples were digested at 90º C in PFA vials using concentrated

HNO_3 and HF, followed by immediate neutralization with 20 g L^{-1} H_3BO_3 to retain Si, as per Cotten et al. (1995). After dilution by a factor of 400, samples were analyzed using an Yvon Horiba Ultima 2 Inductively Coupled Plasma Optical Emission Spectrometer (ICP-OES) calibrated against a standard curve comprised of the CRPG reference materials Mica-Fe, UB-N, MORB-E, GB2, IF-G, AC-E, and WS-E digested in the same batch, using the working values of Govindaraju (1995), and with replicates of IF-G and AC-E treated as unknowns to monitor accuracy. Precision based on 5 replicate analyses was better than 4.5% (2 relative standard deviations, RSD) for all major elements except for Mg, Ca, and Na, which showed lower precision (14 to 21%) between replicates due to their low concentrations in iron formation. For analysis of trace elements and Nd isotopes, between 80 and 120 mg of powder was digested sequentially in PFA vials at 90º C using concentrated HF-HNO_3, aqua regia, and 6M HCl. For trace element analysis, aliquots were resuspended in 2% HNO_3 with indium as an internal standard and analyzed using a Thermo Scientific Element2 High-Resolution Inductively Coupled Plasma Mass Spectrometer (ICP-MS) at the Pôle Spectrométrie Océan in Brest, France. The instrument was tuned to minimize oxide production, and mixed mono-elemental Pr-Nd, Ba-Ce, and Sm-Tb solutions were analyzed to quantify potential oxide interferences prior to the session, which were negligible. Calibration was performed against gravimetrically prepared multi-element solutions, and geostandards IF-G and AC-E were analysed in the same session as unknowns to monitor accuracy, which was better than 5% for REE and 10% for most other trace elements (2 RSD). For major and trace method analyses, detection limits were determined using blanks prepared alongside samples and are reported in Table S2 as either the detected blank concentration (normalized to the typical amount of rock powder analyzed) or the method detection limit determined by three relative standard deviations of the end-of-rinse intensities that were systematically measured prior to each sample. Sm-Nd and La-Ce parent/daughter ratios

were calculated from HR-ICP-MS data of non-spiked samples using $^{147}Sm/^{144}Nd$ = 0.6045 Sm/Nd and $^{138}La/^{142}Ce$ = 0.0080 La/Ce. Propagated relative standard errors on these ratios were constrained to less than 1% by periodic measurements (n=8) of a multi-element solution throughout the session, and to less than 10% for all trace element concentrations, and better than 2–3% for most REE, based on the same repeat analyses.

To assure complete digestion and confirm the REE data acquired after HF-HNO_3-Aqua Regia digestion in PFA beakers, a selected set of sample powders were re-analyzed by HR-ICP-MS after Na_2O_2-NaOH alkaline fusion in glassy carbon crucibles at 650°C in the presence of a Tm spike, following the protocol and data reduction procedure of Bayon et al. (2009).

For Nd isotopes, aliquots were evaporated and re-dissolved in 2.5M HCl for chemical separation of REE using cationic BioRad® AG50X8 200-400 mesh columns, followed by further purification on LnSpec Eichrom resin. Nd isotopic measurements were performed during two analytical sessions at the Pôle de Spectrométrie Océan in Brest using a Thermo Scientific Neptune multi-collector ICP-MS and a Thermo Scientific Triton Thermal Ionisation Mass Spectrometer (TIMS, Triton). A $^{146/144}Nd$ ratio of 0.7219 was used for mass bias correction. Recovered Nd fractions contained between 1266 and 16 ug of Nd (mean 134 ug) while blanks prepared alongside samples contained less than 140 pg of Nd. For TIMS measurements, analyses were made in static mode using 10 blocks of 10 cycles each, with 1 s integration times and baselines measured for 30 s between each block. For MC-ICP-MS measurements, one block of 30 cycles with integration times of 4.196 s was employed, preceded by a 30 s baseline measurement. Results obtained on the international standard JNdi-1 are reported in Table S1. JNdi-1 $^{143}Nd/^{144}Nd$ ratios measured during the TIMS session are slightly lower (0.512086 ± 0.000017, 2 s.d., n=5) than the accepted value obtained using a dynamic routine over a period of 1.5 years on 3 different Triton mass spectrometers (0.512099 ± 0.000005, 2 s.d., n=61, Garçon et

al., 2018). Thus, the measured $^{143}Nd/^{144}Nd$ ratios have been normalized. Aside from correction for instrumental drift using sample-standard bracketing with JNdi-1, no further correction is applied to the Nd isotope ratios during the MC-ICP-MS session since the JNdi-1 results are in agreement with the accepted value (0.512095 ± 0.000005, 2 s.d., n=17).

For Ce isotopes, 100-150 mg of rock powder was digested using a HF-HNO_3 dissolution technique. The chemical separation used to separate the Ce fraction involved four steps of column chemistry (Bonnand et al., 2019). The first step, aimed at removing the Fe fraction, was performed on anionic AG1-X8 resin (100-200 mesh). The sample was loaded onto the resin in strong HCl and Ce was not retained by the resin. The second step was used to separate the REE from other main cations of the matrix. To this end, the samples were loaded in 2.5N HCl onto AG50-X8 resin (200-400 mesh). REE were retained by the resin while major cations were eluted in 2.5N HCl, and REE were then eluted in 6M HCl. The third column procedure was designed to separate Ce^{4+} from other REE and was performed using Ln spec resin (Eichrom). The samples were loaded in 10M HNO_3 + $NaBrO_3$, and Ce^{4+} was retained on the column while other REE were not. The Ce^{4+} fraction was eluted in 6M HCl + H_2O_2. Finally, the samples were processed through the second step to make sure the Ce fraction was cleaned of any remaining matrix cations. Isotopic measurements were performed on a Thermo Scientific Thermal Ionisation Mass Spectrometer (TIMS) at the Laboratoire Magmas et Volcans as described by Bonnand et al. (2019). Together with the samples, Ce_{AMES} and Ce_{LMV} reference materials were analysed and gave $^{138}Ce/^{142}Ce$ values of 0.0225743 ± 0.0000007 (2 s.d.; n=26) and 0.0225705 ± 0.0000006 (2 s.d.; n=48), respectively. The values are comparable to previously published values (e.g. Willbold, 2007).

4. Results

4.1 Major and Trace elements

The Moodies Group BIF are composed of chert, magnetite, and hematite, with minor phyllosilicates (likely stilpnomelane and chamosite), goethite, and rare ankerite (see Table S2 for X-ray diffraction method and data). Samples showed a large range in the concentration of detrital indicators, with Al_2O_3 ranging from 8.5 wt.% to <0.1%, and with correlated concentrations of Sc, Zr, Th, and Hf that reached sub-ppm values in the least contaminated samples (see Tables S3 in the supplementary information for complete elemental dataset). Iron concentrations ranged from 73.8 wt.% Fe_2O_{3Total} to 5.8 wt.%; 43 out of 54 samples meet the definition of iron formation of >15 wt.% Fe (James, 1954), including two samples with Al_2O_3 between 6 and 8 wt.%. Phosphorus concentrations averaged 0.11 wt.% P_2O_5 and no apatite or other P-rich phases were detected by X-ray diffraction nor by μXRF scanning (data not shown). Redox-sensitive trace elements, such as U and Mo, are present at sub-ppm levels. Transition metals (e.g., V, Cr, Mn, Co, Ni, Cu and Zn) show a variability of approximately one order of magnitude in absolute abundances, similar to other larger BIF datasets (Figure S2; e.g., Konhauser et al., 2011; Robbins et al., 2019b).

Shale-normalized (SN) spectra for rare earth elements + yttrium (REY_{SN}; simplified as REE throughout this manuscript) span a wide range in abundances relative to Post-Archean Australian Shale (PAAS; updated values from McLennan, 1989), ranging from below 0.01 to close to 1 (Figure 2). Total REE concentrations show strong correlation with detrital indicators, such as Zr concentrations (Figure 3). REE spectra are highly diverse, with some showing light REE (LREE) enrichment relative to heavy REE (HREE) enrichment, while others show the reverse. Nearly all

samples show suprachondritic Y/Ho ratios, ranging from 20.5 to 45.5, with an average of 35.0, as well as significant positive La and Eu anomalies, and mild positive Gd anomalies. A striking feature of the spectra are highly variable Ce anomalies, with Ce/Ce* reaching values as low as 0.19. A subset of the samples digested by alkaline fusion and analyzed for REE using a Tm spike (Bayon et al., 2009) confirm the large range in La/Ce and Ce/Ce* that is observed for samples digested using concentrated acids in PFA vials (Table S4). The cerium anomaly is calculated here using the formulation of Lawrence et al. (2006) with $Ce/Ce^* = Ce_{SN}/(Pr_{SN} * Pr_{SN}/Nd_{SN})$, where La is not considered in the calculation as to avoid false negative Ce anomalies that may arise simply as the result of La enrichment.

4.2 Nd and Ce isotopes

Nd isotope compositions ($^{143}Nd/^{144}Nd$) of 22 selected samples from all three localities range from 0.510836 to 0.511459, while $^{147}Sm/^{144}Nd$ ratios range from 0.0911 to 0.1453. Nd isotope model ages span 3597 to 2246 Ma, with a mean value of 3161 Ma, assuming a source with CHUR composition ($^{147}Sm/^{144}Nd$=0.1960 and $^{143}Nd/^{144}Nd$=0.512630; Bouvier et al., 2008). Three samples, all from the SB locality, show significantly younger model ages than the rest of the dataset (mean $\tau_{Nd\ CHUR}$ = 2487 Ma); when these three samples are excluded, mean $\tau_{Nd\ CHUR}$ value of the rest of the dataset average 3267 Ma. On a $^{147}Sm/^{144}Nd$ – $^{143}Nd/^{144}Nd$ plot, samples from the SB locality do not show any correlation. Samples from the DSR locality are tightly clustered. With such a small range of Sm/Nd ratios, it is not possible to calculate a robust isochron. Samples from the CC locality show a positive correlation that yields an errorchron with an apparent age of 2770±530 Ma (MSWD=16), considering measured uncertainties.

$^{138}La/^{142}Ce$ ratios for the five DSR samples analyzed range from 0.004 to 0.013, while the SB sample analyzed showed a value of 0.004 (Figure 4b). Cerium isotope compositions ($^{138}Ce/^{142}Ce$) ranged from 0.02257053 to 0.02257522 (Table S5). On a $^{138}La/^{142}Ce$ vs. $^{138}Ce/^{142}Ce$ plot, the five analyzed DSR samples define an isochron that yields an apparent age of 60±32 Ma based on measured uncertainties. The single analyzed SB sample overlaps the range defined by the DSR samples.

5. Discussion

5.1 Unusual REE signatures in Moodies Group BIF

Samples of the shallow-water BIF of the Moodies Group analyzed here show some rather unusual characteristics in their REE systematics. Most striking is the presence of strong Ce anomalies, ranging down to Ce/Ce* = 0.19. Because cerium is readily oxidized from Ce(III) to Ce(IV) in the presence of free oxygen, this process leaves oxic waters depleted in Ce, creating characteristic negative Ce anomalies in oxygenated seawater (shale-normalized Ce anomalies, Ce/Ce*, of about 0.3 – 0.1; e.g., German et al., 1995). BIF deposited before the GOE generally lack Ce anomalies, a feature attributed to the prevalence of anoxic water column conditions (e.g., Bau and Dulski, 1996; Kato et al., 1998). Moodies Group BIF samples show significant Ce anomalies at all three sample locations (Ce/Ce*=0.2 – 0.95; Figure S2), with samples from DSR and SB localities showing the most pronounced anomalies. The magnitude of Ce anomalies observed in our dataset reaches significantly more extreme values than those observed by

Hayashi et al. (2004) in three samples from the Moodies and underlying Fig Tree Groups. One might be tempted to equate these anomalies with oxic Ce cycling at the time of deposition; however, Hayashi et al. (2004) suggested that such anomalies may instead represent post-depositional mobilization of REE with a maximum age of 1.1 Ga.

Another unusual feature of the REE spectra is the highly variable degree of LREE vs. HREE enrichment. Modern seawater, and most detritus-free ancient chemical sediments (both BIF and carbonates; e.g., Bohlar et al., 2004), generally shows HREE enrichment relative to LREE due to lanthanide contraction and the decrease in ionic radii going from LREE to HREE as the result of an increasingly filled f-electron shell. This contraction results in a more important extent of aqueous carbonate complexation for HREE relative to LREE (Lee et al., 1992), leaving a greater proportion of LREE available for adsorption to reactive particle surfaces, thus decreasing their concentration in seawater relative to the more strongly carbonate-complexed HREE. Another consequence of the lanthanide contraction is that LREE are more efficiently mobilized by alteration fluids bearing important REE ligands such as fluoride, phosphate, and carbonate (e.g., Wood, 1990; Bilal and Langer, 1989).

Both syn-depositional and post-depositional processes may influence REE systematics. BIF, however, have generally been considered robust against post-depositional alteration of their REE signatures (Bau, 1993), even by protracted high-grade metamorphism (Bolhar et al., 2004). Nonetheless, the highly atypical nature of the REE signatures observed in this study, and the fact that all samples were obtained from surface outcrop, lead us to examine these assumptions more closely. We first consider controls over REE systematics that can be confidently linked to syn-depositional processes, such as the seawater precipitation of iron and silica chemical components

and the admixture of detrital contaminants, before examining alternative explanations for chemical features that are difficult to explain as primary.

5.1 Syn-depositional control over REE signatures: chemical sedimentation vs. detrital contamination

For the original protolith, prior to any post-depositional alteration, it is reasonable to assume that REE were derived from two contrasting sources; (1) those scavenged directly from seawater onto the surface of the original chemical precipitates, and (2) those delivered physically in association with detrital components. Distinguishing these two sources can be difficult as both primary depositional processes and post-depositional alteration processes have the potential to generate correlations that do not imply causation. For example, total REE concentrations in this dataset show mild but notable correlations with major elements which are typically associated with a predominately chemical sedimentary origin (e.g., Fe, Si, Mn, P; Pearson's correlation coefficients of 0.21, -0.41, 0.28, and 0.59, respectively). However, even stronger correlations are observed between total REE concentrations and the concentrations of detrital indicators (e.g., Al, Ti, Zr, Hf, Th; Pearson's correlation coefficients of 0.91, 0.86, 0.94, 0.91, and 0.95, respectively). A variety of processes may induce such correlations. These include early depositional and diagenetic processes such as REE adsorption to iron oxide precipitates or sequestration of REE into early diagenetic phosphate minerals. However, multiple features of the REE spectra show no relation to the inferred chemical sedimentary component. For instance, there exists no good correlation between Ce/Ce* nor LREE/HREE (evaluated as Nd/Yb, for example) and the concentrations of Fe, Si, Mn, or P.

On the other hand, some features of the REE spectra can be explained by the admixture of detrital components. In order to assess the influence of detrital contributions on REE spectra of the Moodies BIF, we modelled the addition of detrital components to a detritus-poor sample. The chemical composition of the Archean continental crust, used as a detrital component in our model, is highly debated (e.g. Martin et al., 2005). We chose to use an average composition of TTG and Sanukitoids presented in Halla et al. (2017) as representative of the Archean crust and as a material most likely to increase the LREE/HREE slope. The models are presented in Figure 5 and the chemical composition of the detrital component is given in Table S6. As shown in Figure 5a, Moodies samples are characterized by large variations in La/Yb ratios. The addition of detrital material to a detritus-poor sample results in an increase in the La/Yb ratio as shown in Fig. 5a. The model succeeds in reproducing the general trends observed in CC and SB samples but not the high La/Yb ratios in detritus-poor DSR samples. The model also explains variations observed in Yb and Th concentrations (Fig. 5b). This suggests that the increase in Yb in the Moodies samples is primarily controlled by the addition of detrital material. During the addition of detrital material to a detritus-poor sample, the chemical signatures of the REE spectra are modified (Fig. 5c). For example, the LREE depletion, characteristic of detritus-poor samples, is erased by the addition of about 10-15% detrital material. The addition of detrital material also results in the suppression of the positive Y anomaly (Fig. 5c). However, during the addition of detrital material, the positive Eu anomaly is not affected and remains a characteristic feature of detrital-rich samples (Fig. 2). This indicates that the chemical composition of the crustal component is characterized by a positive Eu anomaly, evidence for which is also apparent in Barberton TTG rocks (Moyen et al., 2019, their supplementary data). During the addition of detrital components, the La/Ce and Sm/Nd ratios both decrease slightly.

Detrital contributions can explain large variations in total REE concentrations and also the correlation between Yb and Zr, but fail to explain certain features in the dataset, notably the high La/Yb ratios seen in DSR samples at low Zr abundances, as well as the presence of Ce anomalies in general. As discussed in the next section, these are better explained by post-depositional alteration processes. Detrital contributions appeared to have modified the sensitivity of both of these features (La/Yb and Ce anomalies) to post-depositional alteration.

5.2 Fluid addition

REE spectra have been clearly affected by a secondary process that resulted in differential REE mobilization. Two distinct mechanisms of REE mobilization could be proposed to explain such variations; (1) removal of REE during chemical weathering, and/or (2) addition of REE by fluid circulation. The REE concentrations in aqueous solutions are affected by several parameters, including the original composition of the protolith, the chemical composition of the fluid, and physicochemical conditions during the fluid-rock interaction. For example, during chemical weathering and leaching of REE in basalts, it has been shown that LREE are preferentially mobilized compared to HREE (Cotten et al., 1995). This process results in REE spectra for the fluid that show elevated LREE/HREE ratios relative to the protolith. However, it's important to note that the relative enrichment of LREE and HREE can be highly variable as a function of protolith, fluid chemistry, degree of alteration, . Importantly, during chemical weathering and fluid-rock interaction in tropical environments, Ce is oxidized to Ce^{4+} and becomes insoluble, leaving the fluid with a strong negative anomaly (Cotten et al. 1995). The

removal of REE by chemical weathering would thus result in depletion of the total REE concentration of the protolith, leaving a strong LREE depletion in the residual altered rock and a strong positive Ce anomaly, which is the opposite of what is observed in Moodies BIF. Instead, we propose that fluid addition is largely responsible for generating the unusual REE spectra in the samples. As discussed below, the initial REE content of the iron formations themselves also appears to have played a role in the modification of REE spectra features during fluid addition.

To further explore the possible impact of fluid addition, we have developed two fluid addition models (Fig. 6). The fluid used in these models bears deliberately simple REE spectra and shows two main features; (1) a positive linear enrichment from Lu to La, and (2) a strong negative Ce anomaly (Ce/Ce* = 0.27). The REE concentrations in the model fluid presented in Figure 6 are listed in Table S6. The two models presented in Figure 6 represent the admixing of REE from fluids of the same composition to rocks of differing initial compositions. Two end-member cases are presented where the starting compositions were either detritus-poor or detritus-rich, respectively. During fluid addition, the total REE concentration increases, the REE spectra become progressively enriched in LREE, and negative Ce/Ce* values are produced (Fig. 6). Importantly, the Ce/Yb ratio will either increase or decrease, depending on the composition of the protolith (i.e., detritus-rich or -poor). Similarly, in the case of La/Yb (Figure 5a), detritally contaminated samples (high Zr) do not reach La/Yb ratios above crustal values, whereas detritus-free samples (low Zr) show both high and low La/Yb values. Samples showing low La/Yb values appear to retain the light REE depletion expected for seawater precipitates. However, samples with high La/Yb ratios cannot be explained by a seawater origin nor by detrital contamination; the best explanation for samples found above crustal La/Yb values is late LREE addition.

The REE concentration in the fluid is unknown which prevents us from determining the amount of fluid addition necessary to explain the observed variations. Nevertheless, it is clear that the amount of inherited REE required to alter spectra will be greater for a detritus-rich sample than for a detritus-poor sample. The model we present illustrates the late generation of multiple features of the unusual REE spectra using relatively simple and plausible assumptions, notably a preferential mobility of LREE compared to HREE. It is possible that the source of the mobilized REE is the host rock itself, in which case the fluid would be expected to carry pre-existing anomalies, such as a positive Eu anomaly. However, when considering fluids of different compositions and relative REE mobilities, it quickly becomes apparent that the system is poorly constrained and that diverse fluid compositions may be evoked to explain any given alteration pattern, regardless of the protolith from which REE in the fluids derived. What is apparent, however, is that these fluids were enriched in LREE while at the same time depleted in Ce.

Groundwaters today are characterized by REE concentrations that are generally low, in the nanomolar to picomolar range, including deeper (~200m) groundwaters draining REE-rich lithologies such as granite (Janssen and Verweij, 2003; Noack et al., 2014; Munemoto et al., 2015). Mean iron formation Ce and Pr concentrations observed in our dataset are 10 and 1.3 ppm, respectively. Mass balance indicates that to supply an equivalent amount of REE from groundwater, volumes ranging from as little as 200L per Kg of iron formation, to as much as ten million liters, are implied. Acidic geothermal waters may carry higher REE loads, up to ~0.1 ppm (Wood, 2006), and could supply the necessary REE in as little as 100L per Kg of iron formation. Crucially, the BGB already contains evidence of significant REE mobility during the formation of “ironstone pods” as the result of iron dissolution and reprecipitation in shallow groundwater systems (Lowe and Byerly, 2007). Contrary to the samples studied herein, these pods show a

range of features that are inconsistent with an Archean origin, namely a lack of deformation, stratification aligned with modern topographic slopes, abundant cavities, and goethite drip features. Importantly, these ironstone pods bear both positive and negative Ce anomalies, reaching as low as 0.2 Ce/Ce*, and bear concentrations of REE that are similar to those reported here for the Moodies BIF (Hren et al., 2006). They thus offering an attractive analogue for how significant quantities of REE may have been mobilized under near-surface conditions and with sufficient oxygen exposure to generate large Ce anomalies in markedly older rocks.

5.3 Applicability of Sm-Nd and La-Ce geochronometers for dating fluid addition

As discussed above, fluid addition likely had a strong influence on REE elemental ratios. In Figure 7, we present the impact of our fluid addition model on the La/Ce and Sm/Nd ratios. The La/Ce ratio is most strongly affected because the added fluid is heavily depleted in Ce. This results in an increase in the La/Ce ratio of the altered samples. In the models presented in Figure 7a, the ^{138}La/^{142}Ce ratio evolves from 0.004 to 0.015. During fluid addition, the Sm/Nd ratios are also affected and slightly decrease from 0.13 to 0.10 (Fig. 7b). The modification of parent/daughter elemental ratios during fluid addition has strong implications for the time-dependent evolution of Ce and Nd isotopic compositions because the relatively large variations in La/Ce produced during alteration means that it is possible to use Ce isotopes to constrain the timing of fluid addition.

A large spread in La/Ce ratios, if ancient, should give rise to a corresponding large spread in the ^{138}Ce/^{142}Ce ratio, as sufficient time has passed for ingrowth of ^{138}Ce from ^{138}La decay to occur.

However, if the fractionation of La and Ce is more recent, ingrowth of ^{138}Ce will be small, considering the long half-life of ^{138}La, and samples will show a restricted range in ^{138}Ce/^{142}Ce despite a large apparent range in La/Ce. We have measured the Ce isotopic compositions of six samples with varying ^{138}La/^{142}Ce ratios (from 0.004 to 0.012), and a plot of ^{138}Ce/^{142}Ce versus ^{138}La/^{142}Ce gives an isochron age of 60 ± 32 Ma (Figure 4b). This suggests that the La-Ce elemental fractionation occurred considerably more recently than deposition of the Moodies BIF. In Figure 8a, we report the theoretical isochrons for two fractionation ages (the known 3.2 Ga U/Pb zircon-constrained depositional age, and the La/Ce fractionation age of 1.1 Ga suggested as a maximum age by Hayashi et al., 2004), anchored for simplicity at the same initial ^{138}Ce/^{142}Ce value as indicated by our data. As is clearly evident, the data reported in this study does not show the expected ^{138}Ce ingrowth predicted by a 3.2 Ga isochron, but rather shows a restricted range in ^{138}Ce/^{142}Ce, consistent with a suite of sediments that possessed similar La/Ce ratios for most of their history. This confirms that the La/Ce fractionation is not a primary feature of the Moodies BIF, and crucially, the negative Ce anomalies were generated post-depositionally. Our data also show a less inclined slope than the 1.1 Ga isochron, which contradicts the La/Ce fractionation ages proposed by Hayashi et al. (2004). This maximum age was essentially proposed to explain the radiogenic Ce isotopic composition of a banded ferruginous chert from the Fig Tree Group (εCe=9.2). All our samples, on the contrary, plot on the terrestrial Ce-Nd array defined by Israel et al. (2020) with present day εCe and εNd mean values for the less-perturbed DSR samples of 3.9 and -33.1, respectively.

The fractionation of La from Ce, and thus the generation of negative Ce anomalies, is more recent than proposed by Hayashi et al. (2004). However, considering the long half-life of ^{138}La, we emphasize that the geochronological resolution of our dataset is limited. It is safe to say that

La/Ce fractionation likely occurred in the last 100 Ma. This is consistent with the findings of Lowe and Byerly (2007), who inferred that the "ironstone pods" found in multiple localities in the Barberton Greenstone Belt formed during the Cenozoic, most likely during the Pleistocene. These ironstone pods are composed largely of goethite that would not have survived metamorphic temperatures exceeding ~100 °C without recrystallization to hematite. The BIF sampled in this study also contain a small, but non-negligible, quantity of goethite in some samples (Table S2). This similarly indicates that some hydrological modification must have occurred at near-surface conditions. There appears to be no correlation between the magnitude of the Ce anomaly and any feature of sample mineralogy that would indicate a consistent mineralogical pattern of post-depositional alteration (Table S2). While the Moodies BIF show multiple features consistent with an Archean origin (deformation, strike and dip consistent with adjacent siliciclastic units, mineral assemblages consistent with metamorphosed BIF), it is likely that these units were also subject to hydrological modification during wetter periods of the Cenozoic.

Fluid addition also played a role in the Sm/Nd variations measured in the Moodies BIF, with consequences for Sm-Nd geochronology. In a plot of $^{143}Nd/^{144}Nd$ versus $^{147}Sm/^{144}Nd$, the samples from the CC locality lie on an isochron with an age of 2770 ± 530 Ma whereas the other localities either plot outside of the isochron (most SB samples) or show little variation (DSR). In order to test the influence of fluid addition on the Sm/Nd isochron, we calculated the theoretical 3.2 Ga isochron anchored by the sample with the highest Sm/Nd ratio because this sample was least affected by detrital input or fluid addition, which both act to decrease the Sm/Nd ratio (Figure 8b). It can be clearly seen that the majority of points lie to the left of the theoretical isochron. This is consistent with the models presented where fluid addition is shown to decrease the Sm/Nd ratio and move points to the left of the isochron. The deviation from the 3.2 Ga

isochron can be calculated (as the difference in Sm/Nd ratio expressed in %) and plotted as a function of the magnitude of the cerium anomaly (Figure 9). This deviation scales positively with the magnitudes of negative Ce anomalies in the same samples and is consistent with Sm/Nd ratios that have been affected by fluid addition. However, this fluid delivery did not change the Nd isotope composition. SB samples that are the most affected by the suspected fluid addition show $^{143}Nd/^{144}Nd$ ratios in a narrow range (<2ε), showing that the fluid may have been internal to the examined BIF units.

It is important to note that Sm/Nd ratios are less susceptible to fractionation relative to La/Ce ratios because neither undergo redox transformation under surface or upper-mantle conditions. The shifts in Sm/Nd produced by fluid addition are thus small, and while perceptible on an isochron plot, may still give an isochron age that is within error of the known depositional age (which is the case of the isochron coinciding with the CC samples in Figure 4). Ultimately, while the influence of fluid addition on Sm-Nd geochronology may be apparent, it is unsuitable for resolving the timing of fluid addition due to the muted effects on the Sm/Nd ratio. Sm-Nd geochronology should thus not be used to constrain the timing of emplacement of Ce anomalies in ancient rocks, metasedimentary or otherwise.

5.4 Implications for geochemical proxy reconstruction of Archean redox conditions

Redox-sensitive geochemical proxies such as Ce/Ce* are widely applied to reconstruct the history of Earth surface oxygenation. In Archean black shales, enrichments in redox–sensitive elements (S, Mo, Re, Os), as well as Fe, Mo and C isotopes, all suggest that O_2-rich niches already existed ca. 2.6 to 3.0 Ga (e.g., Wille et al., 2007; Czaja et al., 2012; Stüeken et al., 2012; Thomazo et al., 2013). In diverse metasediments of the Pongola Supergroup, isotope

compositions of S, Fe, Cr, Mo, and U have all similarly been used to indicate the presence of some free O_2 ca. 2.96 Ga ago (Crowe et al., 2013; Planavsky et al., 2014; Wang et al., 2018; Eickmann et al., 2018). Sedimentary Fe isotope composition and U enrichment have also been used to argue for oxygenated surface waters as far back as 3.2 Ga ago (Satkoski et al., 2015).

Nevertheless, a Paleo- to Mesoarchean origin for oxygenic photosynthesis remains controversial (e.g., Johnson et al., 2013; Ward et al., 2016). Part of this controversy is related to alternative interpretations of geochemical records suggested as proxies for O_2 in deep time, especially emerging metal isotope proxies (e.g., Konhauser et al., 2011; Kaufman, 2014) and to uncertainty in the robustness and syngenicity of these signals (Kirschvink et al., 2012; Kaufman, 2014). Indeed, post-depositional oxidation of originally reduced Archean metasediments has been widely demonstrated (e.g., Li et al., 2012; Rasmussen et al., 2014a; Albut et al., 2018). For instance, Hoashi et al. (2009) hypothesized that hematite in the 3.46 Ga Marble Bar chert (Pilbara Supergroup, Australia) occurred as a primary precipitate formed in the presence of seawater, yet this was later discounted on petrographic grounds (Rasmussen et al., 2014b). Similarly, Cr isotope fractionation in the 2.96 Ga Sinqeni IF (Pongola Supergroup, South Africa) that was used to suggest transient atmospheric oxygenation ca. 3.0 Ga (Crowe et al., 2013) was later shown to be present in surface samples but not in fresh drill core (Albut et al., 2018), and since confirmed using U-series isotopic disequilibrium to represent modern weathering (Albut et al., 2019). Due to the uncertainties surrounding the timing of oxidation, it appears that geochemical proxy evidence indicating the former presence of O_2 in water may not alone be sufficient to resolve the debate surrounding the origin of oxygenic photosynthesis.

Several geochemical proxies for O_2 form radiogenic systems that are amenable to dating, and radiogenic approaches for constraining the timing of oxidation have now been successfully

applied using Re-Os (Kendall et al., 2015) and U-Th-Pb (Li et al., 2012; Satkoski et al., 2015). The latter approach provides the only direct geochronological support to date for an oxidative proxy signal dating as far back as 3.2 Ga ago. Our study underlines the necessity of such an approach. Ce/Ce* is considered one of the most robust redox proxies due to the general insolubility of REE at Earth surface conditions, by their immobility during greenschist- and amphibolite-facies metamorphism, and by the fact that Ce becomes even more immobile when oxidized. Indeed, with the exception of the Hayashi et al. (2004) study and this work, we are unaware of any reports of confirmed late emplacement of negative Ce anomalies in Archean-aged metasedimentary rocks. However, several published datasets in Archean rocks warrant reexamination of the inferred syn-depositional origin of negative Ce anomalies. For example, an Archean paleosol from the Singhbhum Craton displays strongly negative Ce anomalies that were used to suggest transient atmospheric oxygenation sometime prior to 3.02 Ga, yet iron loss and U immobility within the paleosol, as well as the presence of redox-sensitive detrital pyrite and uraninite in overlying sediments, indicate reducing conditions (Mukhopadhyay et al., 2014). Furthermore, the sample showing the most pronounced Ce anomaly conspicuously shows pronounced LREE enrichment but comparable Ce abundance relative to other samples. In a study compiling REE data from multiple studies, Kato et al. (2006) highlighted that several different BIF occurrences deposited prior to 2.5 Ga are characterized by negative Ce anomalies. It would be prudent to re-examine these samples for telltale signs of REE mobilization and the generation of Ce anomalies by fluid addition, which may be indicated by LREE enrichment. While late emplacement of a negative Ce anomaly by an alteration fluid simply requires oxic conditions at some point during the fluid's trajectory, it's important to note that this anomaly could persist if conditions became anoxic further along the flow path. Contrary to some redox indicators such as uranium that are rapidly scrubbed out of solution at reductive redox boundaries (c.f. Abdelouas et

al., 2000, and reference therein), only dilution by non-fractionated REE, or possibly reductive dissolution of minerals that already bore a positive Ce anomaly, would erase a negative Ce anomaly from an alteration fluid. Such a scenario may lead to the emplacement of negative Ce anomalies in rocks that simultaneously bear indicators of anoxia, such as U immobility.

This work constitutes a cautionary tale in that even the most robust (e.g., least easily reset) elemental and isotopic proxies for ancient oxygenation, such as REE and their isotopes, are susceptible to post-depositional alteration. In the case of REE-based proxies, as described here, there are a variety of supplemental indicators that can be used to reveal such processes, such as modifications to the REE spectra and perturbation to Nd and Ce isotope systematics. This is not the case for all elemental and isotopic redox proxies. Therefore, when inferring the ancient presence of O_2 from elemental and isotopic redox proxies, additional confirmatory information regarding the syn-depositional nature of the signal is required.

6. Conclusion

Some BIF of the Moodies Group show unusual features in their shale-normalized REE spectra, most notably pronounced negative Ce anomalies and variable LREE vs. HREE enrichment, with some samples possessing LREE that are enriched compared to HREE. We examined the origin of these features with respect to potential syn- and post-depositional processes that may have influenced the REE spectra. While total REE abundances scale weakly with the concentrations of elements that were likely derived from the chemical components of the sediment (Fe, Si, Mn, P), there appears to be little relation between their concentrations and the features of the REE spectra

themselves. By contrast, total REE abundances scaled strongly in a positive fashion with the concentrations of indicators of detrital contamination, notably Al, Ti, Hf, Th, and Zr. Detrital contamination clearly exerted control over REE features in these samples but cannot explain the presence of significant negative Ce anomalies nor extreme LREE enrichments relative to HREE, which we attribute to post-depositional mobilization of REE and addition of REE by alteration fluids. A simple model for the late addition of REE can explain these unusual spectral features for both detritus-rich and detritus-poor samples. The influence of this late REE addition is also evident in the Ce and Nd isotope systematics of these samples. La/Ce ratios were significantly altered by fluid addition, and the samples form a La-Ce isochron that constrains the timing of fluid addition to within the last 100 Ma. This is consistent with previous suggestions that negative Ce anomalies in ferruginous sediments of the Barberton Greenstone Belt are not primary features and confirms the utility of the La-Ce isotope approach for constraining the timing of oxidation as expressed by the Ce anomaly redox proxy. Sm/Nd ratios were less perturbed by fluid addition; nevertheless, the effect of fluid addition is evident in the Nd isotopic compositions of the samples, with deviation of both the sample set Sm-Nd isochron, as well as Nd model ages, that is proportional to the importance of fluid addition, as inferred by the magnitude of the negative Ce anomaly. This work highlights the need for careful consideration of the potential for post-depositional alteration to modify elemental and isotopic redox proxies. Caution is warranted when inferring the ancient presence of O_2 in the absence of direct geochronological constraints on the age of the proxy signal.

References

Abdelouas, A., Lutze, W., Gong, W., Nuttall, E.H., Strietelmeier, B.A., Travis, B.J. Biological reduction of uranium in groundwater and subsurface soil. Science of the Total Environment 250, 21–35 (2000).

Albut, G., Babechuk, M. G., Kleinhanns, I. C., Benger, M., Beukes, N. J., Steinhilber, B., Smith, A. J. B., Kruger, S. J., Schoenberg, R. Modern rather than Mesoarchaean oxidative weathering responsible for the heavy stable Cr isotopic signatures of the 2.95 Ga old Ijzermijn iron formation (South Africa). Geochimica et Cosmochimica Acta 228, 157–189 (2018).

Albut, G., Kamber, B.S., Brüske, A., Beukes, N.J., Smith, A.J.B., Schoenberg, R. Modern weathering in outcrop samples versus ancient paleoredox information in drill core samples from a Mesoarchaean marine oxygen oasis in Pongola Supergroup, South Africa. Geochimica et Cosmochimica Acta 265, 330–353 (2019).

Anhaeusser, C.R. The geology of the Sheba Hills area of the Barberton Mountain Land, South Africa, with particular reference to the Eureka Syncline. Transactions of the Geological Society of South Africa 79, 253-280 (1976).

Bau, M., Effects of syn- and post-depositional processes on the rare-earth element distribution in Precambrian iron-formations. European Journal of Mineralogy 5, 257-267 (1993).

Bau, M., Dulski, P. Distribution of yttrium and rare-earth elements in the Penge and Kuruman iron-formations, Transvaal Supergroup, South Africa. Precambrian Research 79, 37-55 (1996).

Bayon, G., Barrat, J.A., Etoubleau, J., Benoit, M., Bollinger, C., Révillon, S. Determination of Rare Earth Elements, Sc, Y, Zr, Ba, Hf and Th in Geological Samples by ICP-MS after Tm Addition and Alkaline Fusion. Geostandards and Geoanalytical Research 33, 51–62 (2009).

Bekker, A., Slack, J. F., Planavsky, N., Krapež, B., Hofmann, A., Konhauser, K. O. & Rouxel, O. J. Iron Formation: The Sedimentary Product of a Complex Interplay among Mantle, Tectonic, Oceanic, and Biospheric Processes. Economic Geology 105, 467–508 (2010).

Bilal, B. A., Langer, P. Complex formation of trace elements in geochemical systems: stability constants of fluorocomplexes of the lanthanides in a fluorite bearing model system up to 200 °C and 1000 bar. Inorganica Chimica Acta 140, 297–298 (1987).

Bolhar, R., Kamber, B., Moorbath, S., Fedo, C., Whitehouse, M. Characterisation of early Archaean chemical sediments by trace element signatures. Earth and Planetary Science Letters 222, 43–60 (2004).

Bonnand, P., Israel, C., Boyet, M., Doucelance, R., Auclair, D. Radiogenic and stable Ce isotope measurements by Thermal Ionisation Mass Spectrometry. Journal of Analytical Atomic Spectrometry, accepted (2019).

Byrne, R.H., Sholkovitz, E.R. Chapter 158. Marine chemistry and geochemistry of the lanthanides. In: Gschneidner Jr., K. A., LeRoy, E. (Eds.), Handbook on the Physics and Chemistry of Rare Earths. Elsevier, pp. 497–593 (1996).

Cotten, J., Le Dez, A., Bau, M., Caroff, M., Maury, R.C., Dulski, P., Fourcade, S., Bohn, M., Brousse, R. Origin of anomalous rare-earth element and yttrium enrichments in subaerially exposed basalts: Evidence from French Polynesia. Chemical Geology 119, 115-138 (1995).

Crowe, S.A., Døssing, L.N., Beukes, N.J., Bau, M., Kruger, S.J., Frei, R., Canfield, D.E. Atmospheric oxygenation three billion years ago. Nature 501, 535-538 (2013).

Czaja, A. D., Johnson, C.M., Roden, E.E., Berad, B.L., Voegelin, A.R., Nägler, T.F., Beukes, N.J., Wille, M., Evidence for free oxygen in the Neoarchean ocean based on coupled iron–molybdenum isotope fractionation. Geochimica et Cosmochimica Acta 86, 118–137 (2012).

Eickmann, B., Hofmann, A., Wille, M., Bui, T.H., Wing, B.A., Schoenberg, R.,. Isotopic evidence for oxygenated Mesoarchaean shallow oceans. Nature Geoscience 11, 133-138 (2018).

Frost, C., von Blanckenburg, F., Schoenberg, R., Frost, B., Swapp, S. Preservation of Fe isotope heterogeneities during diagenesis and metamorphism of banded iron formation. Contributions to Mineralogy and Petrology 153, 211–235 (2007).

Garçon, M., Boyet, M., Carlson, R. W., Horan, M. F., Auclair, D., Mock, T. D. Factors influencing the precision and accuracy of Nd isotope measurements by thermal ionization mass spectrometry. Chemical Geology 476, 493–514 (2018).

German, C.R., Masuzawa, T., Greaves, M.J., Elderfield, H., Edmond, J.M. Dissolved rare earth elements in the Southern Ocean: Cerium oxidation and the influence of hydrography. Geochimica et Cosmochimica Acta 59, 1551–1558 (1995).

Govindaraju, K. 1995 Working values with confidence limits for twenty-six CRPG, ANRT, and IWG-GIT Geostandards. Geostandards and Geoanalytical Research 19, 1–32 (1995).

Halla, J., Whitehouse, M. J., Ahmad, T., Bagai, Z. Archaean granitoids: an overview and significance from a tectonic perspective. Geological Society London Special Publications 449, 1–18 (2017).

Hayashi, T., Masaharu, T., Tsuyoshi, T. Origin of negative Ce anomalies in Barberton sedimentary rocks, deduced from La–Ce and Sm–Nd isotope systematics. Precambrian Research 135, 345-357 (2004).

Heubeck, C., Lowe, D. R. Depositional and tectonic setting of the Archean Moodies Group, Barberton Greenstone Belt, South Africa. Precambrian Research 68, 257-290 (1994).

Heubeck, C. The Moodies Group - A high-resolution archive of Archaean surface and basin-forming processes; In *The Archaean Geology of the Kaapvaal Craton, Southern Africa*. Springer (Regional Geology Reviews), 203-241 (2019).

Heubeck, C., Engelhardt, J., Byerly, G.R., Zeh, A., Sell, B., Luber, T., Lowe, D.R. Timing of deposition and deformation of the Moodies Group (Barberton Greenstone Belt, South Africa): Very-high-resolution of Archaean surface processes. Precambrian Research 231, 236- 262 (2013).

Hoashi, M., Bevacqua, D.C., Otake, T., Watanabe, Y., Hickman, A.H., Utsunomiya, S., Ohmoto, H. Primary haematite in an oxygenated sea 3.46 billion years ago. Nature Geosciences 2, 301–306 (2009).

Israel, C., Boyet, M., Doucelance, R., Bonnand, P., Frossard, P., Auclair, D., Bouvier, A. Formation of the Ce-Nd mantle array: Crustal extraction vs. recycling by subduction. Earth and Planetary Science Letters 115941 (2019). doi:10.1016/j.epsl.2019.115941

James, H.L. Sedimentary facies of iron-formation. Economic Geology 49, 235-293 (1954).

Janssen, R.P.T., Verweij, W. Geochemistry of some rare earth elements in groundwater, Vierlingsbeek, The Netherlands. Water Research 37, 1320–1350 (2003).

Johnson, J.E., Webb, S.M., Thomas, K., Ono, S., Kirschvink, J.L., Fischer, W.W. Manganese-oxidizing photosynthesis before the rise of cyanobacteria. Proceedings of the National Academy of Sciences of the United States of America 110, 11238–11243 (2013).

Kato Y., Ohta I., Tsunematsu T., Watanabe Y., Isozaki Y., Maruyama S. and Imai N. Rare earth element variations in mid-Archean banded iron formations: implications for the chemistry of ocean and continent and plate tectonics. Geochimica et Cosmochimica Acta 62, 3475–3497. (1998)

Kato, Y., Yamaguchi, K. E., Ohmoto, H. Rare earth elements in Precambrian banded iron formations: Secular changes of Ce and Eu anomalies and evolution of atmospheric oxygen. In *Evolution of Early Earth's Atmosphere, Hydrosphere, and Biosphere - Constraints from Ore Deposits* 57**,** 187–23 (Geological Society of America, 2006).

Kaufman, A.J. Early Earth: Cyanobacteria at work. Nature Geoscience 7, 253–254 (2014).

Kendall, B., Creaser, R. A., Reinhard, C. T., Lyons, T. W. & Anbar, A. D. Transient episodes of mild environmental oxygenation and oxidative continental weathering during the late Archean. Science Advances 1, e1500777 (2015).

Kirschvink, J.L., Raub, T.D., Fischer, W. Archean “whiffs of oxygen” go Poof! Goldschmidt Conference. Mineralogical Magazine A1943 (Montreal) (2012).

Konhauser, K.O., Lalonde, S.V., Planavsky, N.J., Pecoits, E., Lyons, T.W., Mojzsis, S.J., Rouxel, O.J., Barley, M.E., Rosìere, C., Fralick, P.W., Kump, L.R., Bekker, A. Aerobic bacterial pyrite oxidation and acid rock drainage during the Great Oxidation Event. Nature 478, 369–373 (2011).

Konhauser, K. O., Planavsky, N. J., Hardisty, D. S., Robbins, L. J., Warchola, T. J., Haugaard, R., Lalonde, S. V., Partin, C. A., Oonk, P. B. H., Tsikos, H., Lyons, T. W., Bekker, A., Johnson, C. M. Iron formations: A global record of Neoarchaean to Palaeoproterozoic environmental history. Earth Science Reviews 172, 140–177 (2017).

Kröner, A., Byerly, G.R., Lowe, D.R. Chronology of early Archean granite–greenstone evolution in the Barberton Mountain Land, South Africa, based on precise dating by single zircon evaporation. Earth Planetary Science Letters 103, 41–54 (1991).

Lawrence, M.G., Greig, A., Collerson, K.D., Kamber, B.S. Rare Earth Element and Yttrium Variability in South East Queensland Waterways. Aquatic Geochemistry 12, 39–72 (2006).

Lee, J.H., Byrne, R.H. Complexation of trivalent rare earth elements (Ce, Eu, Gd, Tb, Yb) by carbonate ions. Geochimica et Cosmochimica Acta 57, 295–302 (1992).

Li, W., Czaja, A.D., van Kranendonk, M.J., Beard, B.L., Roden, E.E., Johnson, C.M. An anoxic, Fe(II)-rich, U-poor ocean 3.46 billion years ago. Geochimica et Cosmochimica Acta 120, 65–79 (2012).

Lowe, D.R., Byerly, G.R. Ironstone bodies of the Barberton greenstone belt, South Africa: Products of a Cenozoic hydrological system, not Archean hydrothermal vents! Geological Society of America Bulletin 119, 65–87 (2007).

Martin, H., Smithies, R.H., Rapp, R., Moyen, J.-F., Champion, D. An overview of adakite, tonalite–trondhjemite–granodiorite (TTG), and sanukitoid: relationships and some implications for crustal evolution. Lithos 79, 1-24 (2005).

McLennan, S. Geochemistry and mineralogy of rare earth elements. Reviews in Mineralogy 21, 169-200 (1989).

Mongelli, G. Rare-earth elements in Oligo-Miocenic pelitic sediments from Lagonegro Basin, southern Apennines, Italy: implications for provenance and source area weathering. International Journal of Earth Science (Geol Rundsch) 1–9 (2004). doi:10.1007/s00531-004-0401-z

Moyen, J.-F., Stevens, G., Kisters, A. F. M., Belcher, R. W., Lemirre, B. TTG Plutons of the Barberton Granitoid- Greenstone Terrain, South Africa. In *Earth's Oldest Rocks*, 615–653 (Elsevier, 2019).

Mukhopadhyay, J., Crowley, Q.G., Ghosh, S., Ghosh, G., Chakrabarti, K., Misra, B., Heron, K., Bose, S. Oxygenation of the Archean atmosphere: New paleosol constraints from eastern India. Geology 42, 923–926 (2014).

Munemoto, T., Ohmori, K., Iwatsuki, T. Rare earth elements (REE) in deep groundwater from granite and fracture-filling calcite in the Tono area, central Japan: Prediction of REE fractionation in paleo- to present-day groundwater. Chemical Geology 417, 58–67 (2015).

Noack, C.W., Dzombak, D.A., Karamalidis, A.K. Rare Earth Element Distributions and Trends in Natural Waters with a Focus on Groundwater. Environmental Science & Technology 48, 4317–4326 (2014).

Planavsky, N.J., Asael, D., Hofmann, A., Reinhard, C.T., Lalonde, S.V., Knudsen, A., Wang, X., Ossa Ossa, F., Pecoits, E., Smith, A.J.B., Beukes, N.J., Bekker, A., Johnson, T.M., Konhauser, K.O., Lyons, T.W., Rouxel, O.J. Evidence for oxygenic photosynthesis half a billion years before the Great Oxidation Event. Nature Geoscience 7, 283–286 (2014).

Posth, N.R., Koehler, I., Swanner, E., Schröder, C., Wellmann, E., Binder, B., Konhauser, K.O., Neumann, U., Berthold, C., Nowak, M., Kappler, A. (2013). Simulating Precambrian banded iron formation diagenesis. Chemical Geology, 362, 131-142.

Rasmussen, B., Krapež, B., Meier, D.B. Replacement origin for hematite in 2.5 Ga banded iron formation: Evidence for postdepositional oxidation of iron-bearing minerals. Geological Society of America Bulletin 126, 438–446 (2014a).

Rasmussen, B., Krapez, B., Muhling, J.R. Hematite replacement of iron-bearing precursor sediments in the 3.46-b.y.-old Marble Bar Chert, Pilbara craton, Australia. Geological Society of America Bulletin 126, 1245–1258 (2014b).

Robbins, L.J., Funk, S., Flynn, S.L., Warchola, T.J., Li, Z., Lalonde, S.V., Rostron, B.J., Smith, J.B., Beukes, N.J., de Kok, M.O., Heaman, L.M., Alessi, D.S., and Konhauser, K.O., 2019. Hydrogeological constraints on the formation of Palaeoproterozoic banded iron formations. Nature Geoscience, 12:558-563.

Robbins, L.J, Konhauser, K.O., Warchola, T.J., Homann, M., Thoby, M., Foster, I., Mloszewska, A.M., Alessi1, D.S, and Lalonde, S.V. A comparison of bulk versus laser ablation trace element analyses in banded iron formations: Insights into the mechanisms leading to compositional variability. Chemical Geology, 506, 197-224 (2019b).

Satkoski, A.M., Beukes, N.J., Li, W., Beard, B.L., Johnson, C.M. A redox-stratified ocean 3.2 billion years ago. Earth and Planetary Science Letters 430, 43–53 (2015).

Stüeken, E.E., Catling, D.C, Buick, R. Contributions to late Archaean sulphur cycling by life on land. Nature Geoscience 5, 722–725 (2012).

Thomazo, C., Papineau, D. Biogeochemical Cycling of Nitrogen on the Early Earth. Elements 9, 345-351 (2013).

Tice, M.M., Bostick, B.C., Lowe, D.R. Thermal history of the 3.5-3.2 Ga Onverwacht and Fig Tree Groups, Barberton greenstone belt, South Africa, inferred by Raman microspectroscopy of carbonaceous material. Geology 32, 37-40 (2004).

Toulkeridis, T., Goldstein, S.L., Clauer, N., Kröner, A., Lowe D.R. Sm-Nd dating of Fig Tree clay minerals of the Barberton greenstone belt, South Africa. Geology 22, 199-202 (1994).

Toulkeridis, T., Goldstein, S.L., Clauer, N., Kröner, A., Todt, W., Schidlowski, M. Sm–Nd, Rb–Sr and Pb–Pb dating of silicic carbonates from the early Archaean Barberton Greenstone Belt, South Africa:

Evidence for post-depositional isotopic resetting at low temperature. Precambrian Research 92, 129-144 (1998).

Wang, X., Planavsky, N.J., Hofmann, A., Saupe, E.E., De Corte, B.P., Philippot, P., Lalonde, S.V., Jemison,
N.E., Zou, H., Ossa, F.O., Rybacki, K., Alfimova, N., Larson, M.J., Tsikos, H., Fralick, P.W., Johnson, T.M., Knudsen, A.C., Reinhard, C.T., Konhauser, K.O. A Mesoarchean shift in uranium isotope systematics. Geochimica et Cosmochimica Acta 238, 438–452 (2018).

Ward, L.M., Kirschvink, J.L., Fischer, W.W. Timescales of Oxygenation Following the Evolution of Oxygenic Photosynthesis. Origins of Life and Evolution of Biospheres. 46, 51-65 (2016).

Willbold, M. Determination of Ce isotopes by TIMS and MC-ICPMS and initiation of a new, homogeneous Ce isotopic reference material. Journal of Analytical Atomic Spectrometry, 22 1364–1372 (2007).

Wille, M., Kramers, J.D., Nägler, T.F., Beukes, N.J., Schröder, S., Meisel, Th., Lacassie, J.P., Voegelin, A.R. Evidence for a gradual rise of oxygen between 2.6 and 2.5 Ga from Mo isotopes and Re-PGE signatures in shales. Geochimica et Cosmochimica Acta 71, 2417–2435 (2007).

Wood, S. A. The aqueous geochemistry of the rare-earth elements and yttrium. Chemical Geology 88, 99–125 (1990).

Wood, S.A. Rare earth element systematics of acidic geothermal waters from the Taupo Volcanic Zone, New Zealand. Journal of Geochemical Exploration 89, 424–427 (2006).

Acknowledgments:

This work was supported by Deutsche Forschungsgemeinschaft (DFG) grant KO5111/1-1 to I.K., DFG grant He2418/13–1 to C.H., and LabexMER ANR-10-LABX-19 and EU Prestige COFUND-GA-2013-609102 grants to M.H. S.V. L. and M.B. acknowledge support from the European Union's Horizon 2020 research and innovation programme (grant agreement no 716515 to S.V.L. and grant agreement no 682778 to M.B.). K.K. acknowledges support from NSERC discovery grant RGPIN-165831. We thank C. Bosq, D. Auclair, J.-L. Piro, C. Liorzou, M.-L. Rouget, B. Gueguen, and E. Ponzevera for assistance with major, trace, and isotopic analyses.

Declaration of competing interest:

We have no competing financial interests or personal relationship that could have appeared to influence the work reported in this paper.

Figures

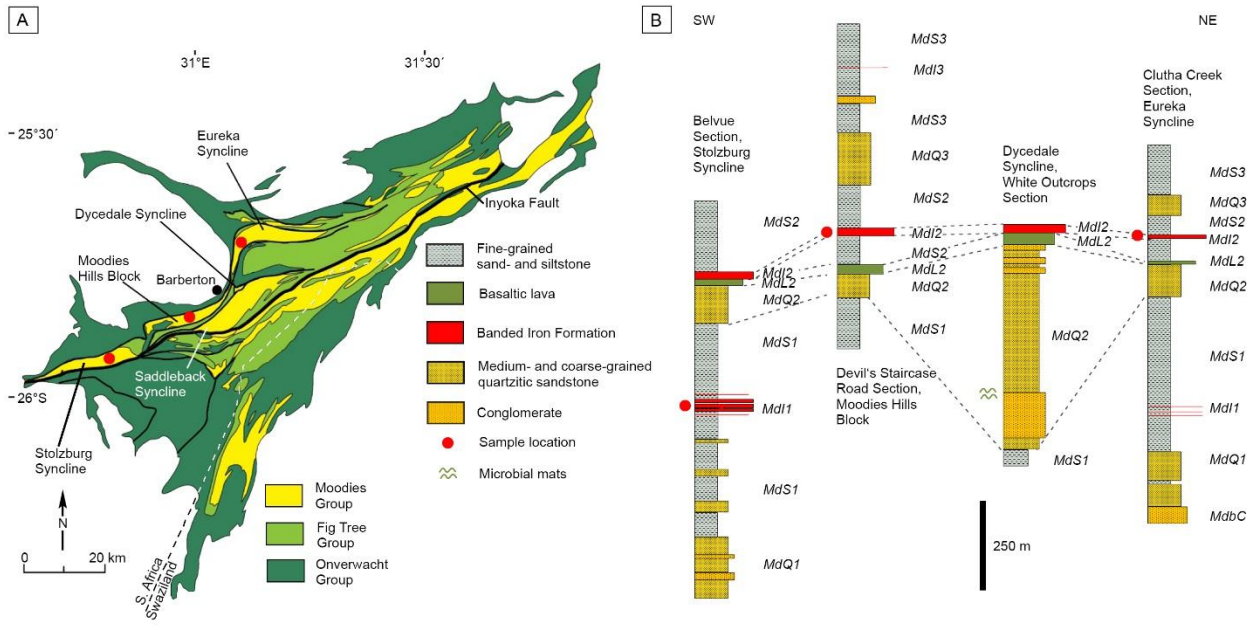

Figure 1. Location and stratigraphy of Moodies Group BIF in the Barberton Greenstone Belt. (A) Map showing sampling locations. (B) Stratigraphic columns of the Stolzburg Syncline, Moodies Hills Block, Dycedale Syncline and Eureka Syncline. Abbreviations of stratigraphic units follow Anhaeusser (1976).

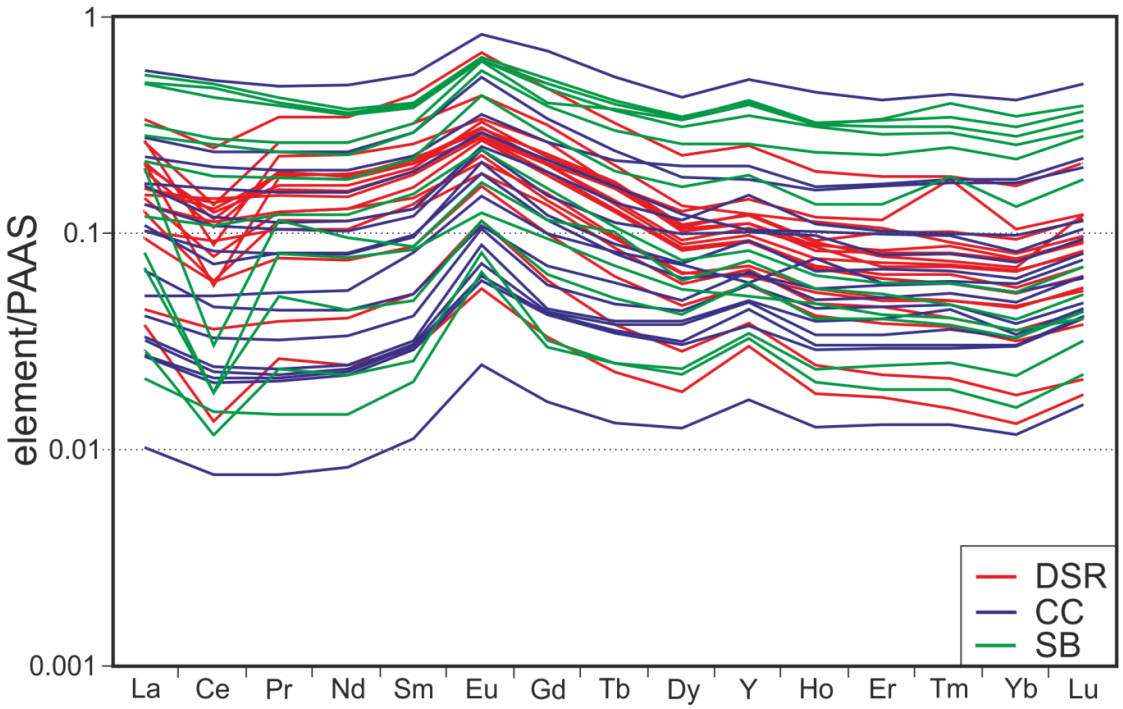

Figure 2. PAAS-normalized REE patterns of Moodies BIF analysed in this study (DSR = Devil's Staircase Road of the Moodies Hills block, CC = Clutha Creek section of the Eureka Syncline, SB = eastern Stolzburg Syncline).

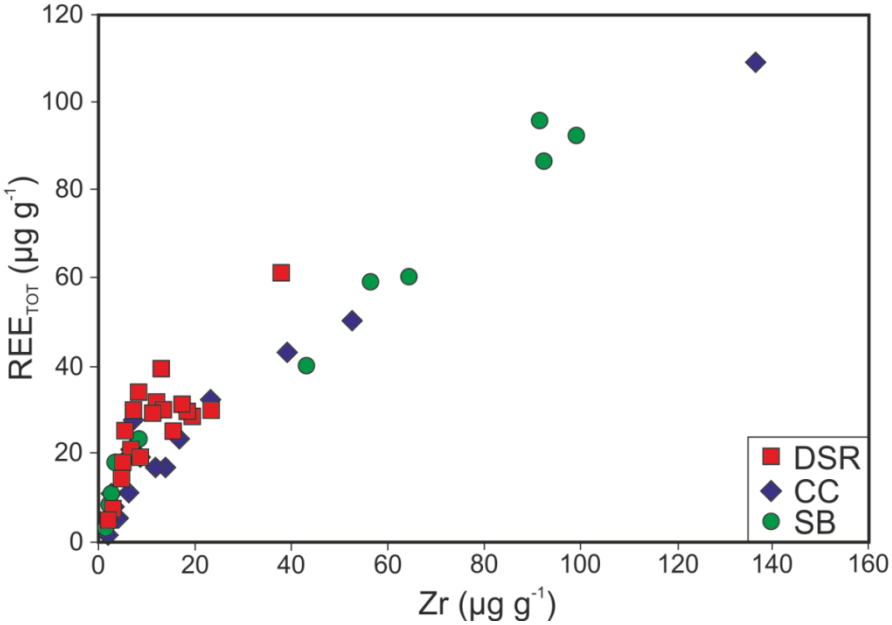

Figure 3. Total REE content versus Zr content in the Moodies BIF. Abbreviations as in Fig. 2.

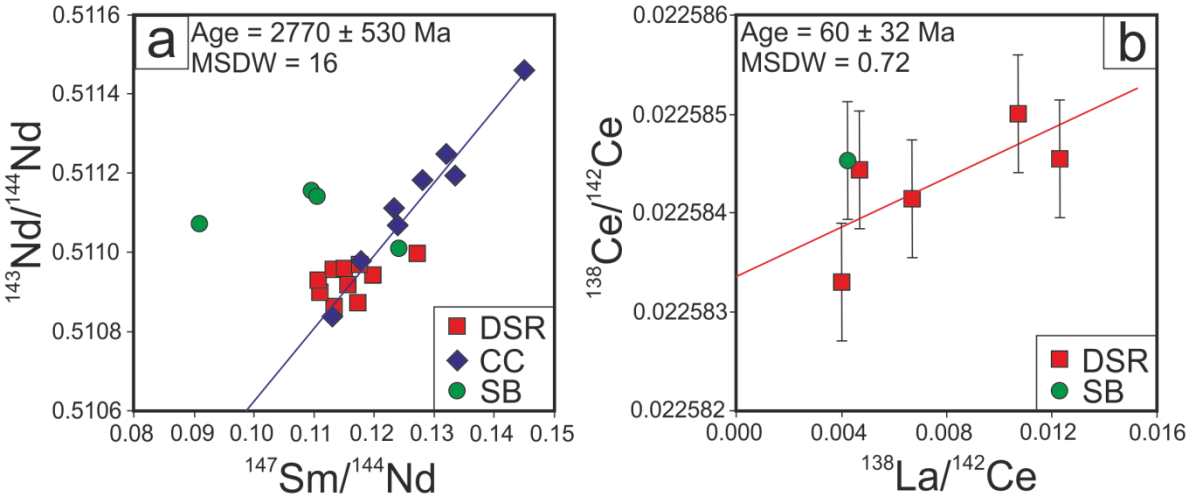

Figure 4. (a) Sm-Nd isotope composition of Moodies Group BIF analysed in this study. (b) La-Ce isotope composition of selected samples from the SB and DSR localities.

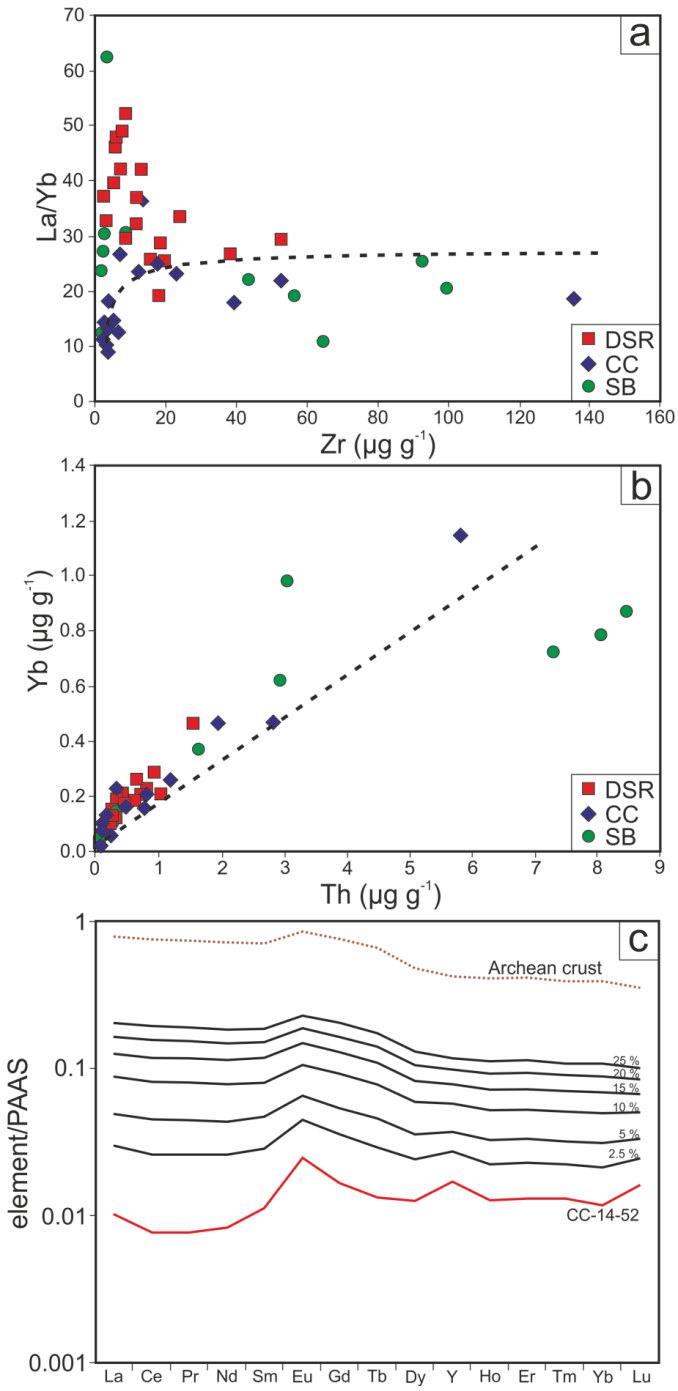

Figure 5. (a) La/Yb ratio versus Zr concentrations for Moodies Group BIF. (b) Yb concentration versus Th concentration of the Moodies Group BIF. (c) PAAS-normalized REE patterns for a detritus-poor sample (CC-14-52) together with models of admixture of detrital input. Dashed lines in (a) and (b) represent the admixing model of detrital material. Values for Archean Crust in (c) are from Halla et al. (2017) (Table S6). The values given in (c) show the amount of detrital material added to the detritus-poor sample. See text for details.

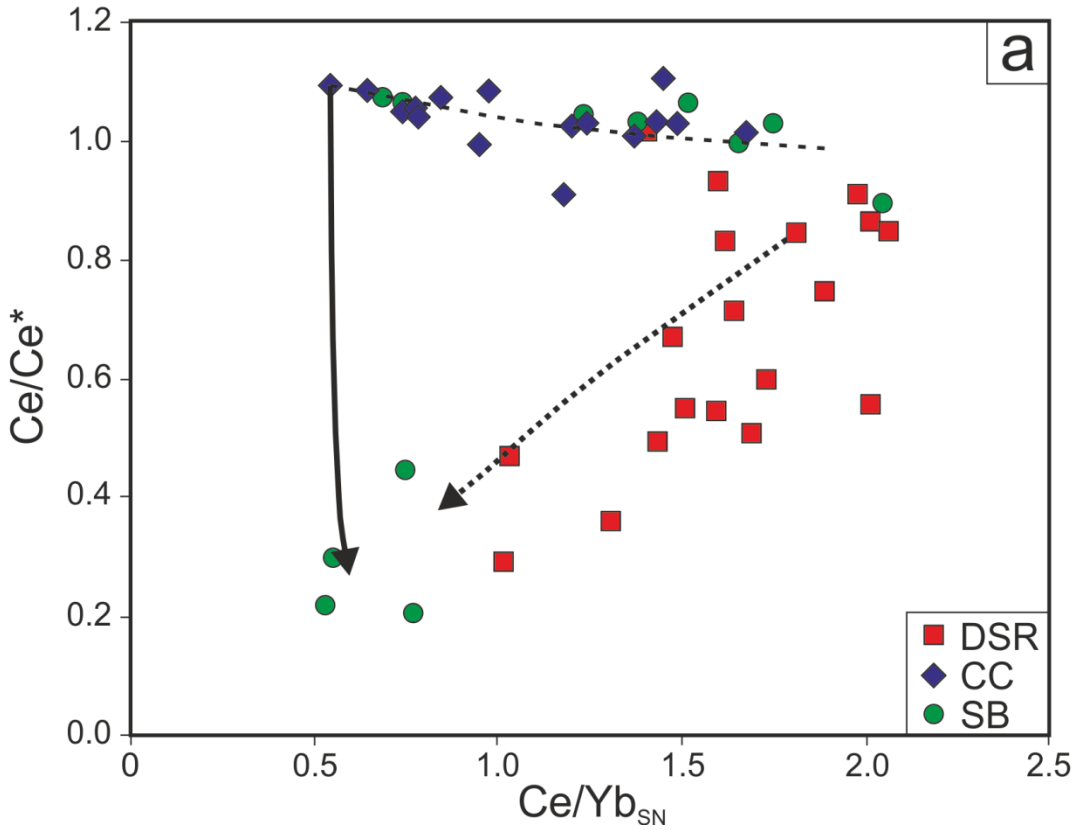

Figure 6. Ce anomaly versus shale-normalised Ce/Yb ratio in Moodies Group BIF. The dashed line represents the admixing model; arrow indicates increasing admixture of detrital material. The dotted and solid lines show fluid addition models with detritus-poor and detritus-rich starting composition, respectively. See text for details.

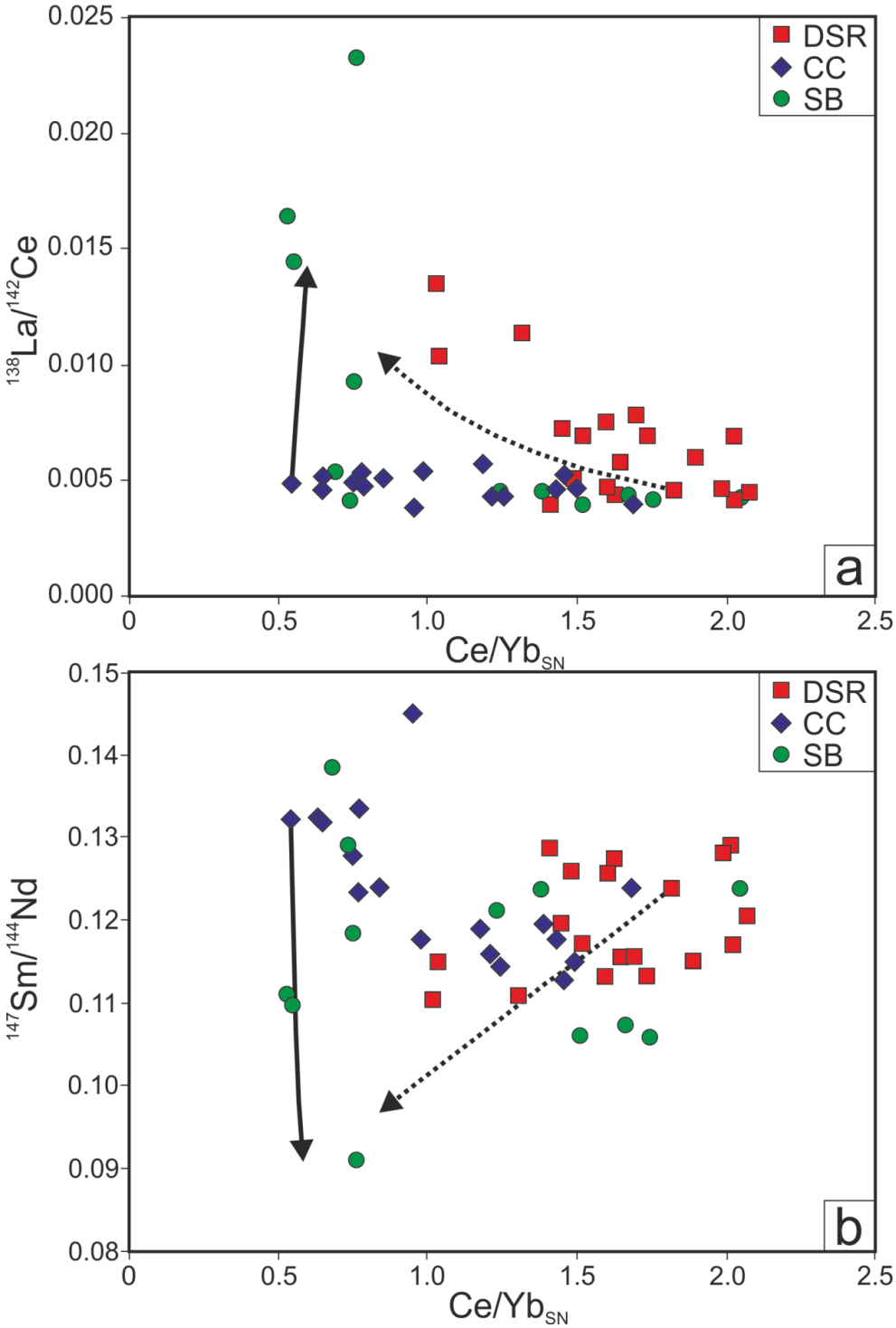

Figure 7. (a) ^{138}Ce/^{142}Ce versus shale-normalized Ce/Yb ratio. (b) ^{147}Sm/^{144}Nd versus shale-normalized Ce/Yb ratio in the Moodies Group BIF analysed in this study. The dotted and solid lines show fluid addition models with a detritus-poor and detritus-rich starting composition, respectively. See text for details.

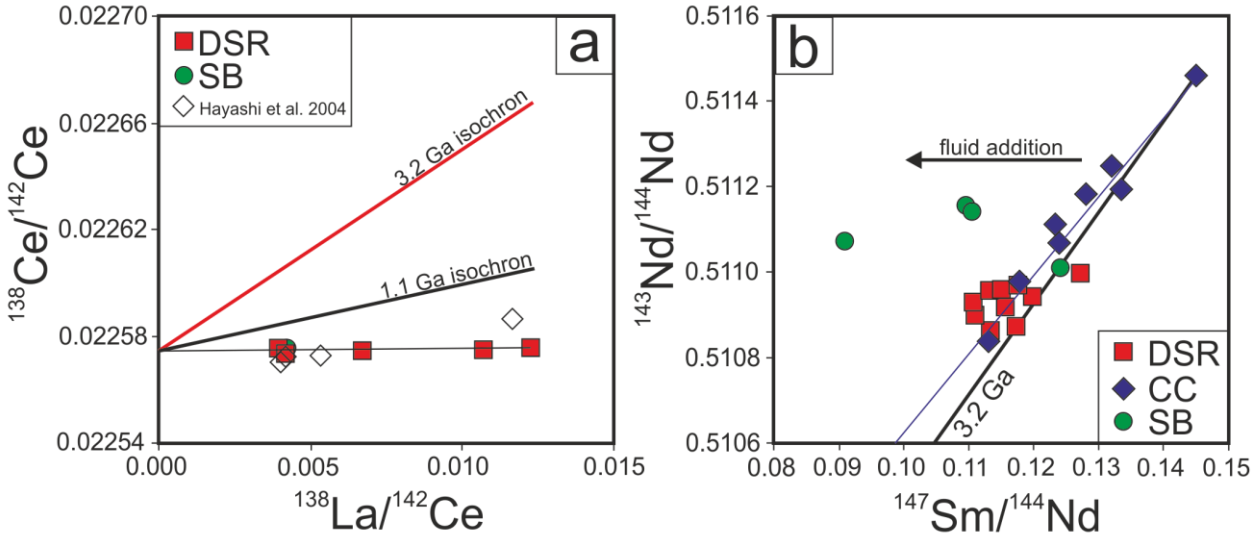

Figure 8. (a) La-Ce isotope composition of selected samples from the SB and DSR localities; (b) Sm-Nd isotope composition of Moodies Group BIF analysed in this study. In (a), the black and red lines are theoretical Sm-Nd isochrons at 1.1 Ga and 3.2 Ga, respectively. In (b), the blue line is the isochron calculated using samples from the CC locality only;the black line is a theoretical isochron calculated using the U/Pb-constraineddepositional age. The arrow in (b) indicates the modification induced by fluid addition.

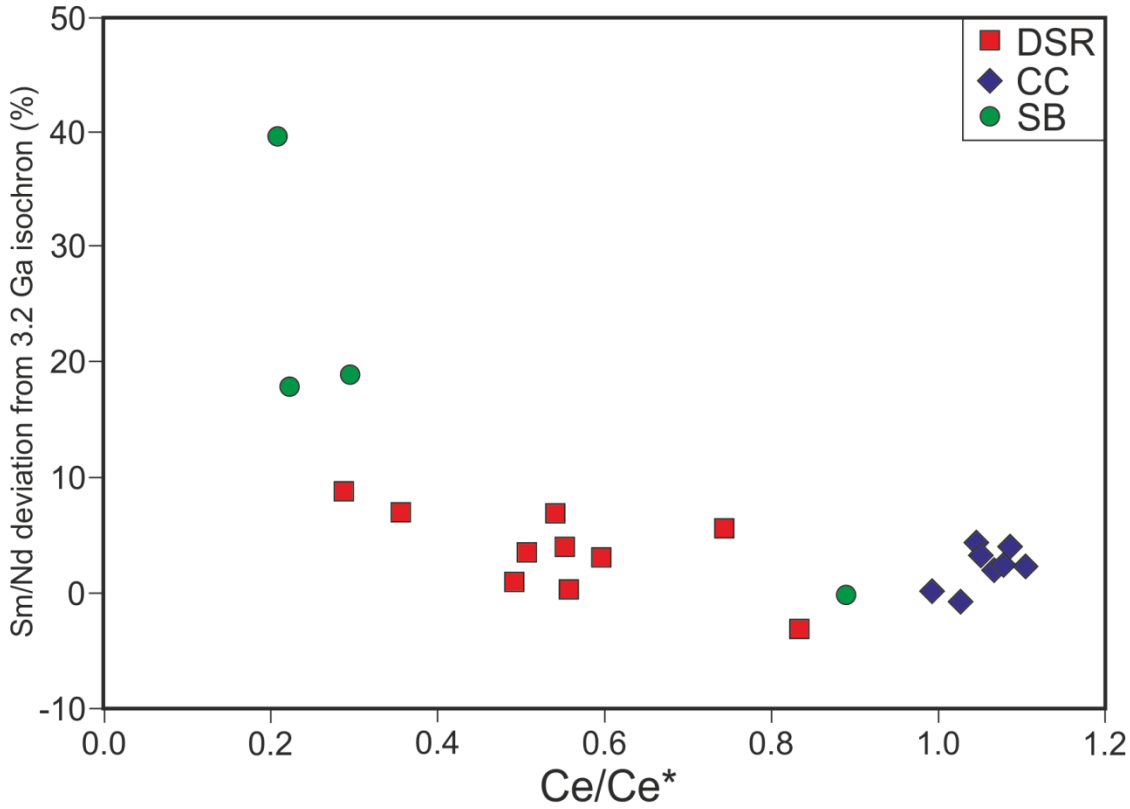

Figure 9. Degree of Sm/Nd-ratio deviation from the 3.2 Ga isochron (in %) versus magnitude of the Ce anomaly of Moodies Group BIF. See text for details.

Supplementary Figures

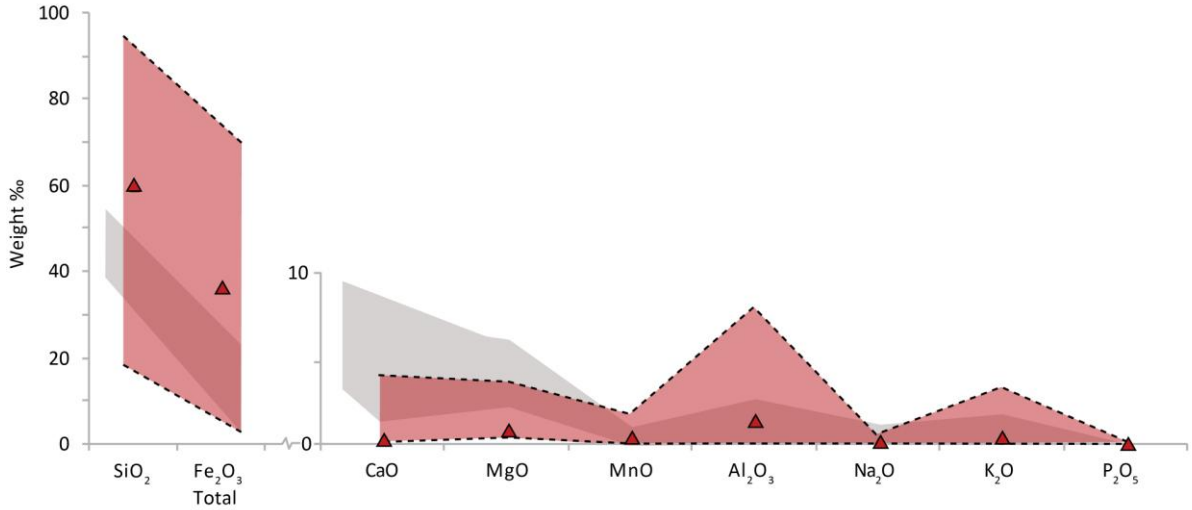

Figure S1. Mean (triangles) as well as maximum and minimum concentrations (red shaded area) of major elements in Moodies Group BIF (n=48). For comparison (gray shaded area), the range of values provided by Klein (2005) for a large compilation of Archean and Paleoproterozoic BIF (n=90).

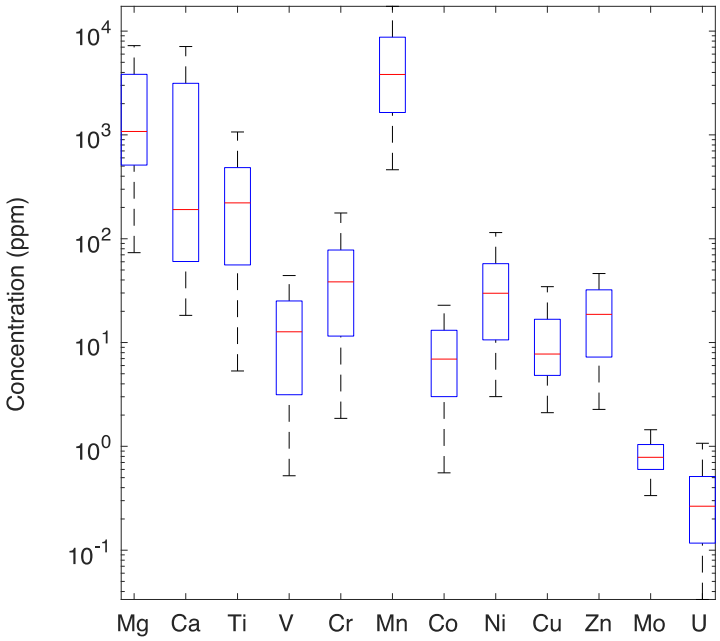

Figure S2. Box-and-whisker plot of selected major elements and transition metals in Moodies Group BIF (n=51). Red lines represent mean values, box limits denote 75th and 25th percentiles, and whiskers show the full range of values.

Reference

Klein, C., 2005 Some Precambrian banded iron-formations (BIFs) from around the world: Their age, geologic setting, mineralogy, metamorphism, geochemistry, and origin. Am. Mineral. 90, 1473–1499.